Bioinspiration & Biomimetics

RECEIVED
10 October 2017

REVISED
25 January 2018

ACCEPTED FOR PUBLICATION
12 February 2018

PUBLISHED
27 March 2018

PAPER

Surface wave energy absorption by a partially submerged bio-inspired canopy

C Nové-Josserand[1], F Castro Hebrero[2], L-M Petit[1], W M Megill[3], R Godoy-Diana[1] and B Thiria[1]

[1] Laboratoire de Physique et Mécanique des Milieux Hétérogènes (PMMH), CNRS UMR 7636, ESPCI Paris—PSL Research University, Sorbonne Universités—Université Pierre et Marie Curie—Paris 6, Université Paris Diderot—Paris 7, 10 rue Vauquelin, 75005 Paris, France
[2] Laboratorio de Fluidodinámica (LFD), Facultad de Ingeniería, Universidad de Buenos Aires (CONICET), Av. Paseo Colón 850, C1063ACV, Buenos Aires, Argentina
[3] Faculty of Technology and Bionics, Rhine Waal University of Applied Sciences, Kleve, Germany

E-mail: clotilde.nove-josserand@espci.fr

Keywords: wave damping, surface waves, wave-structure interactions, elasticity

Abstract

Aquatic plants are known to protect coastlines and riverbeds from erosion by damping waves and fluid flow. These flexible structures absorb the fluid-borne energy of an incoming fluid by deforming mechanically. In this paper we focus on the mechanisms involved in these fluid-elasticity interactions, as an efficient energy harvesting system, using an experimental canopy model in a wave tank. We study an array of partially-submerged flexible structures that are subjected to the action of a surface wave field, investigating in particular the role of spacing between the elements of the array on the ability of our system to absorb energy from the flow. The energy absorption potential of the canopy model is examined using global wave height measurements for the wave field and local measurements of the elastic energy based on the kinematics of each element of the canopy. We study different canopy arrays and show in particular that flexibility improves wave damping by around 40%, for which half is potentially harvestable.

1. Introduction

The energy in ocean waves is considerable and is especially evident when the water gets shallow near the shore. Coastal erosion is a major concern in many cases, and flooding prevention is a high priority for land use planners in vulnerable coastal regions. Studies of aquatic vegetation such as salt marshes or kelp have shown that natural flexible structures can withstand and dissipate the energy carried ashore by ocean waves (Koehl and Wainwright 1977, Koehl 1984, Dubi and Torum 1994, Denny and Gaylord 2002, Buck and Buchholz 2005). Denny and Gaylord (2002) reviewed the mechanics of wave-swept marine algae in order to understand how these plants can survive such forces, by looking at their size, shape and their interaction with the surrounding flow. While many aquatic organisms develop into small and tough objects, and tend to live in relative shelter on the sea floor, marine macroalgae (such as kelp) extend their long, flexible stipes to the surface of the water, where the wave energy is the highest and the hydrodynamic forces are the largest. Their ability to live in these rough conditions is in part thanks to their capacity to reconfigure (Vogel 1984, 1989). These plants can passively alter their shape in order to become more streamlined and reduce any drag forces imposed by the incoming flow, which suggests that the flexibility of the plant material plays a key role in their survivorship. A similar mechanism is evident in terrestrial vegetation subject to wind (see De Langre (2008), for a review).

The mechanisms involved in the reconfiguration of vegetation subject to fluid flow have been the focus of a number of recent studies (see e.g. Barsu *et al* 2016, Leclercq and de Langre (2016), Luhar and Nepf (2016)). This is especially interesting when looking at sediment transport (Järvelä *et al* 2006) and coastal erosion (Feagin *et al* 2009, Manca *et al* 2012). It has been observed that when flow passes through a vegetation field—which we refer to as canopy (Nepf 2012)—, the kinetic energy of the fluid is transferred to the plant through mechanical bending, which results in a damping of the flow. Experimental studies have investigated the interaction of flow over a bed of vegetation (Dubi and Torum 1996, Løvås and Tørum 2001, Anderson and Smith 2014, Möller *et al* 2014). In particular, Augustin *et al* (2009) compared wave dissipation through emergent and near-emergent vegetation fields, and found the former to be more effective by 50%–200% per wavelength, due to the larger wave energy at the surface of the water. Nonetheless, both experimental data and field data provide varied results (Anderson *et al* 2011), and the role played by each parameter in these systems with strong fluid-structure interaction couplings is yet to be studied in more detail.

Several models have been developed for vegetation motion under wave-forcing in order to predict hydrodynamic forces and quantify wave energy dissipation (Asano *et al* 1992, Dubi and Torum 1994, Massel *et al* 1999, Henry *et al* 2015, Luhar and Nepf 2016), but these are limited as there is not yet a universally-accepted model for describing plant movement. Therefore, most studies base their results on fitted bulk drag coefficients (Luhar and Nepf 2016).

The most recent and complete model developed in Zeller *et al* (2014) is capable of simulating finite-amplitude deflections while accounting for drag and added mass. This model demonstrated that the drag generated by the vegetation motion depends strongly on the ratio of blade tip excursion to wave orbital excursion. More recently, Luhar and Nepf (2016) presented a simple, predictive framework to account for blade motion in wave energy dissipation models, based on experimental and numerical work. The results showed that for certain values of Cauchy number, which represents the ratio of the hydrodynamic forcing to the restoring force due to blade stiffness, the flexible blades exerted larger hydrodynamic forces than their rigid equivalent, possibly due to a vortex shedding that is yet missing in the simple model. Concerning hydrodynamic forces, the role of the canopy density is crucial because of the sheltering effect, as demonstrated recently in the experimental work of Barsu *et al* (2016). The spacing between elements in a model canopy will be the experimental parameter under scrutiny in the present paper. A number of works have addressed the problem of water wave diffraction by arrays of vertical structures (see e.g. Kagemoto and Yue (1986), Linton and Evans (1990)), leading to the evaluation of forces related to trapped modes within the rigid array (Kakuno and Liu 1993, Duclos and Clément 2004, Kamath *et al* 2015). Wave diffraction has also been considered as a result of a localised area of wave energy dissipation, a global perspective where the damping is a result of local energy losses due to a cluster of cylinders (Dalrymple *et al* 1984). Mei *et al* (2011, 2014) developed a semi-analytic theory for predicting wave propagation through patches of rigid emergent cylinders, which was later adapted to periodic arrays and circular forests (Guo *et al* 2014, Liu *et al* 2015) and extended to heterogenous forests (Chang *et al* 2017a, 2017b). The theory models turbulence with a constant eddy viscosity that is based on measured values of drag forces. These models, therefore, depend on experimental data and fitted factors.

Most studies focusing on wave energy dissipation by aquatic vegetation consider the context of protecting shorelines or understanding the hydrodynamics of the nearshore currents, rather than on how this dissipated energy could potentially be harvested. Regarding wave energy harvesting, works have been mostly directed at existing or developing technologies, such as the study by Sarkar *et al* (2014) on the Aquamarine Oyster device. This numerical work has looked at predicting the hydrodynamic behaviour of such devices when placed in a row or back to back. It aimed to study specifically the effects of spatial arrangements on the wave energy absorption efficiency. The principal observations conclude that as devices are placed further away from each other, these tend to behave as single units and therefore oscillate more, which benefits the amount of energy harvested. On the other hand, placing devices back to back was found to create destructive interferences causing each device to oscillate much less, leading to lower efficiency in the system. The present study aims to build on these predicted behaviours in order to improve our understanding of the interaction of wave-driven fluid motion and an array of flexible vegetation-inspired structures, with a focus on how the wave energy is distributed in such a system. Particular interest is given to the estimation of energy harvesting potential of the bending of our structures and their consequent de-energising effect on the wave-driven flow.

2. Methods

The experimental set-up consisted of an array of flexible slender blades subjected to a surface water wave field created in a small-scale laboratory wave canal 1.5 m wide and 4.3 m long, as represented in figure 1. A linear wave maker moving vertically was used to create controlled monochromatic waves and an angled polymer (PVC) sheet was placed at the end of the canal to act as a beach and minimise wall reflections.

The natural resonant frequency of the blades was measured equal to 4.5 Hz using a simple free oscillation test in water. Therefore, the imposed frequency of the wave maker was chosen to range from 2 Hz to 5 Hz. Dimensions of the water tank were chosen to fit capillary-gravity dispersion conditions, for a water depth of 8 cm. At the chosen frequency range, the conditions also match deep water conditions and, so, group velocity is assumed to equal half phase velocity. The imposed wave conditions are summarised in table 1 below.

The blades were made from Mylar® material of thickness 350 μm, density 1380 kg $\cdot$ m^{-3} and Young's Modulus (E) 5 GPa. Individual Mylar® blades were fixed to Lego® blocks, which were arranged on a Lego® base board. Each block-blade element could then be easily fixed and removed from the common base to

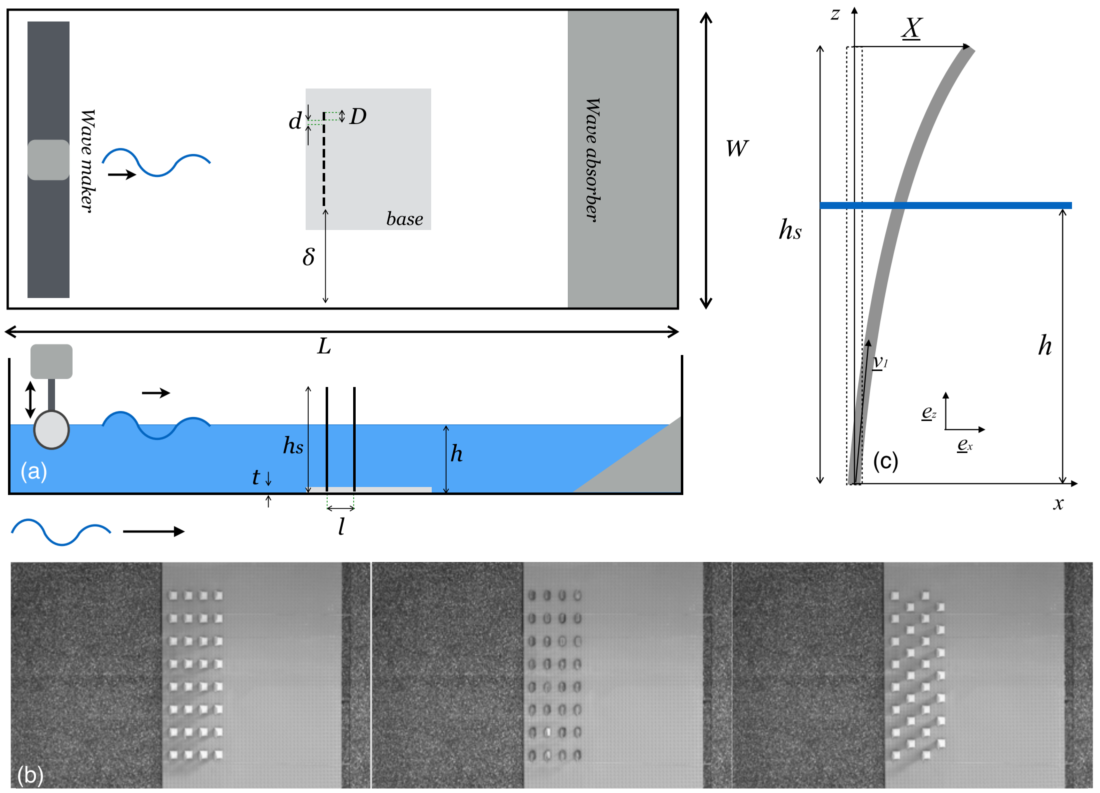

Figure 1. (a) Experimental set-up sketch. (b) Typical images from the experiment for configuration of R_4 flexible aligned (left), R_4 rigid aligned (middle), and R_4 flexible staggered (right). (c) Sketch of a cantilevered beam model.

create the desired blade arrangements. Blades were 14 mm wide and 12 cm long. Aspect ratio, defined as width over length, was $D/h_s = 0.12$ (see figure 1). To study the influence of blade spatial distribution on the wave energy distribution, three types of experiments were run:

1. varying the number $\mathcal{R}$ of rows, for fixed l and d,
2. varying the distance l, for fixed d and $\mathcal{R}$,
3. varying the distance d, for fixed l and $\mathcal{R}$.

Values of l and d were varied between $0.06 - 1.11\lambda$ and $0.03 - 0.92\lambda$, respectively. For each frequency, a reference case without blades (*Control*) was also run. A summary of the configurations is listed in table 1. To investigate the role of flexibility on wave energy damping, additional experiments were conducted using rigid blades of the same dimensions, cut from 2 mm thick plexiglas sheets. All configurations presented in table 1 were repeated with the rigid blades, along with an equivalent flexible staggered configuration for which the space l was kept identical. An example of all three case for configuration R_4 is presented in figure 1(b). All experiments were run using the same base board, 65.5 cm wide by 35 cm long. For both l and d configurations, the total number of blades was fixed to 32 (8 blades per row) in order to separate the influence of these two space parameters independently from the number of blades.

A partially submerged configuration was chosen in order to allow for maximal interaction between the incoming waves and the blades. With a water depth of 8 cm, the submergence ratio was $h_s/h = 1.38$. The average incident wave amplitude η varied between 0.7 and 3.5 mm, depending on the frequency of the wavemaker. Finally, the distance δ separating the edge of the array from the edge of the wave tank was chosen to be sufficiently large compared to the water wave lengths, in order to avoid strong lateral reflections and any subsequent diffraction within the array (see table 2).

In order to provide a realistic model of a potential wave energy converter (WEC) system, the dimensionless numbers of our reduced model in the laboratory must have the same order of magnitude as a planned prototype of oscillating blades in the sea. The Keulegan–Carpenter (KC) number quantifies the oscillatory forcing applied by waves on an obstacle and it is therefore commonly used to characterise WEC systems. It is defined as $\mathrm{KC} = \frac{UT}{D}$, with U being the wave particle horizontal velocity, T the wave period, and D the characteristic length of our object (its width in our case) (Keulegan 1958). This reduces to $\mathrm{KC} = 2\pi\frac{\eta}{D}$ in the case of sinusoidal waves and deep water conditions, thereby becoming the ratio between the wave amplitude and the obstacle width. Given the dimensions of our blades and the amplitudes of our waves, the values of KC produced in the laboratory range between [0.3–1.57] (see table 2). In real seas, wave amplitudes range between

Table 1. Configurations tested for varying number of rows, distance l in between rows, and distance d within rows.

Name	$\mathcal{R}$	l (cm)	d (cm)	l/λ	d/λ	δ/λ
1. Increasing number of rows						
R_1	1	3.2	3.4	[0.09–0.44]	[0.09–0.47]	[1.57–7.74]
R_2	2	↓	↓	↓	↓	↓
R_3	3					
R_4	4					
2. Increasing distance l						
l_1	4	2.4	3.4	[0.06–0.33]	[0.09–0.47]	[1.57–7.74]
l_2	↓	3.2	↓	[0.09–0.44]	↓	↓
l_3		4.0		[0.11–0.55]		
l_4		4.8		[0.13–0.67]		
l_5		5.6		[0.15–0.78]		
l_6		6.4		[0.18–0.89]		
l_7		7.2		[0.20–1.00]		
l_8		8.0		[0.22–1.11]		
3. Increasing distance d						
d_1	4	2.4	1.0	[0.06–0.33]	[0.03–0.14]	[1.87–9.20]
d_2	↓	↓	1.8	↓	[0.05–0.25]	[1.77–8.72]
d_3			2.6		[0.07–0.36]	[1.67–8.23]
d_4			3.4		[0.09–0.47]	[1.57–7.74]
d_5			4.2		[0.11–0.58]	[1.47–7.25]
d_6			5.0		[0.14–0.69]	[1.37–6.76]
d_7			5.8		[0.16–0.81]	[1.17–6.27]
d_8			6.6		[0.18–0.92]	[1.17–5.78]

Table 2. Experimental conditions: frequency f, amplitude η, wave lengths λ, with phase v_ϕ and group v_g velocities of imposed waves.

f (Hz)	η (mm)	λ (cm)	v_ϕ (m s^{-1})	v_g (m s^{-1})	KC
2	1.8	35.24	0.70	0.35	0.80
2.5	3.5	25.4	0.63	0.32	1.57
3	1.9	18.56	0.55	0.28	0.9
3.5	2.3	13.96	0.48	0.24	1.03
4	1.2	10.8	0.43	0.21	0.45
4.5	1	8.72	0.39	0.20	0.43
5	0.7	7.16	0.35	0.18	0.29

[1–5 m], which would impose a width of $\mathcal{O}(10–20)$ m for real scale blades, in order to maintain similar values of KC. Such sizes are coherent with the dimensions of existing WECs, such as Aquamarine's Oyster device which is 18 m wide (Sarkar *et al* 2014). Reynolds number defined as $\mathrm{Re} = \frac{\rho UD}{\mu}$ is used to compare inertial forces to friction forces. In the case of oscillatory flow, the characteristic velocity U is once again taken as the maximum amplitude of oscillation of the water particles (orbital velocity at the free surface), which, in sinusoidal waves can simplify to $u = \omega\eta$. From table 2, this gives values ranging from $\mathrm{Re} = [286 - 770]$.

In order to avoid canal reflections, each experiment was analysed over the period of the first travelling waves only. As shown in figure 2, the array is subject to both wave-maker and beach reflections, which both can distort the resulting behaviour of our system. Therefore, we chose to work in a restrictive time frame for which no reflections have yet reached the recording area of the camera. For each frequency tested, camera recordings were launched as the motor was started and these were taken over 500 images. For each test, a spatio-temporal plot was drawn using the software package ImageJ®, making it possible to determine the specific frame at which the first full wave has travelled through the array and reached the end of the recording area (x_1) (see figure 3). From the known wave characteristics and canal dimensions, one could then calculate the total number of frames over which the analysis could be done while remaining free of reflections.

With a starting distance d_{start} of 1.91 m and an ending distance d_{end} of 4.46 m, and with a fast camera acquisition frequency of 30 fps, it was calculated that the lowest frequency of 2 Hz allowed for a working window of 217 frames following the calculated t_{begin}. The analysis was performed over 100 images and began at the measured t_{begin}. These restrictions correspond to 7–16 wave periods and allowed for large error margins (see table 3 for details).

The surface wave maps were then calculated using the Schlieren method developed by Moisy *et al* (2009). This non-intrusive method relies on the analysis of refracted images of a known pattern, placed at the bottom of the canal bed. The apparent deformed images are then visualised and recorded through the transparent fluid using a fast camera placed above the water surface, and are compared to the reference image taken with a flat water surface. Each recorded image of size 1935 × 1216 pixels is then analysed using the PIVlab algorithm running on MATLAB® and based on stand-

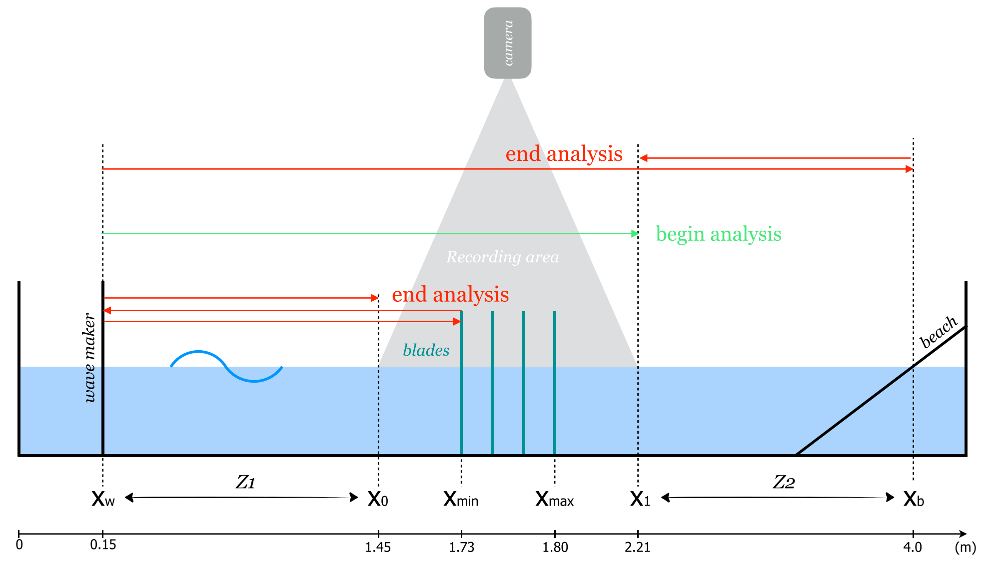

Figure 2. Sketch of analysis restrictions.

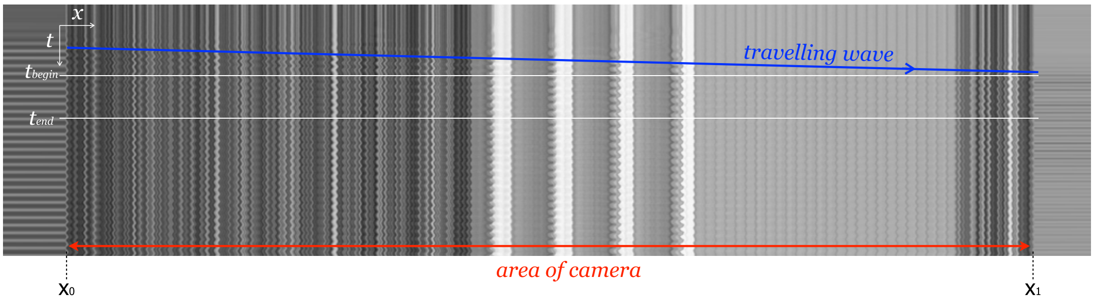

Figure 3. Illustration of the method for measuring t_{begin}, using a spatio-temporal plot of the travelling wave.

Table 3. Summary of recording characteristics for all tested frequencies.

f (Hz)	v_g (m s^{-1})	t_{begin} (s)	t_{end} (s)	$\#T_{\text{analysis}}$	Margin (%)
2	0.35	5.42	12.66	7	53
2.5	0.32	6.02	14.04	8	58
3	0.28	6.86	16.02	10	63
3.5	0.24	7.82	18.26	11	68
4	0.21	8.84	20.65	13	71
4.5	0.21	9.74	22.73	15	74
5	0.18	10.67	24.92	16	76

ard direct image correlation algorithms (DIC). Due to the correlation steps of analysis, the final treated images of the surface waves provide an image precision of 1.58 mm px^{-1}. An example of the treated images is given in figure 4.

The second part of the analysis was focused on the bending of the blades, which relies on the recording of the beam movements. The top of each blade was painted black to contrast with surroundings and the movement of each blade end was quantified using a spatio-temporal stacking method as provided by the software package ImageJ, (see figure 8). It was thus possible to track the movement of each blade using the same recorded images as those used for the surface wave maps, thereby ensuring that the data for both parts of the analysis sprung from identical experiments.

3. Results and discussion

Conservation of energy within our system imposes that the total energy of the incoming waves is shared between reflection, transmission and dissipation within the array. This energy analysis is performed in two parts: the first part focuses on the study of the surface wave maps (3.1) in order to determine reflection and transmission coefficients while the second part focuses on the mechanics of the blade array (3.2) in order to determine dissipation coefficients. Finally, both are combined in order to evaluate the energy distribution within our system.

3.1. Surface wave maps

For each configuration listed in table 1, the surface wave maps were studied before and after the blade array, as presented in figure 4(c). Although the Moisy correlation technique is designed to work with a

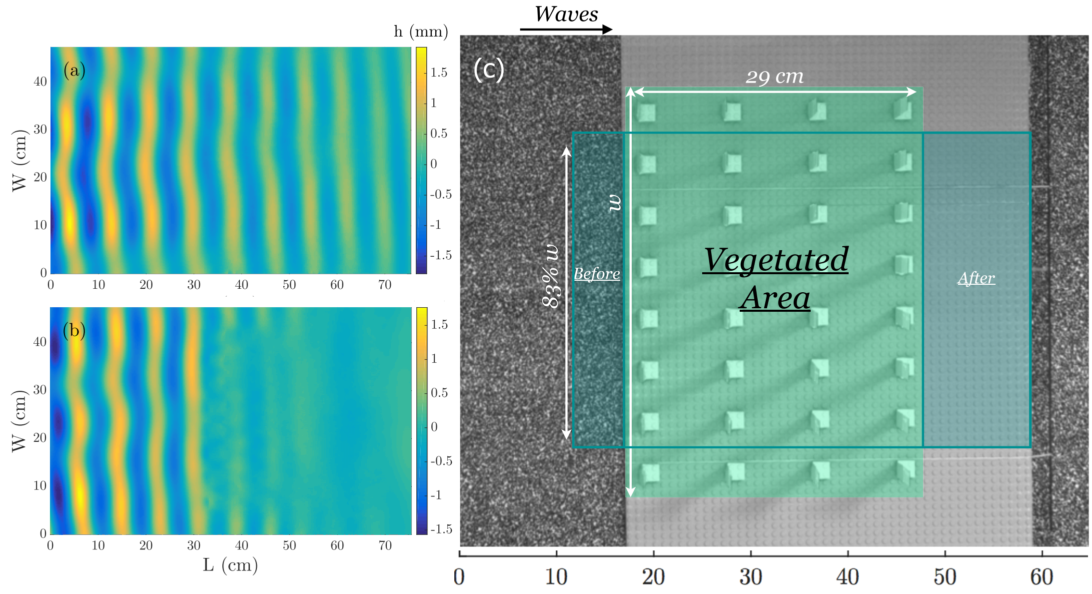

Figure 4. Typical surface wave maps obtained with the Schlieren method for *Control* (a) and configuration l_2 (b). Zones of analysis for transmission and reflection coefficients (c).

background pattern of random dots, we chose to work also in the area of our lego base, in order to extend the zone of analysis a little further. For the correlation function, the images of reference were taken before each one of the studied configurations, so that the dotted lego base blade also served as the element of comparison. Therefore, the wave maps were calculated before the array using the random pattern and after the array using the base. Although, the latter is less accurate, (the surface elevations obtained are 30% lower due, in part, to the lower light contrast), the ensuing method for calculating the transmission and reflection coefficients described below was carefully chosen in order to overcome these inaccuracies.

In the specific case of configuration d, the surface elevation maps had to be analysed over an adapted area in order to remain coherent throughout our study. Indeed, for larger d spacings, part of the vegetated area exceeded the camera view. Therefore, in order to maintain comparable results, the width w of the area of analysis was varied, depending on the configuration's d spacing. The visible ratio of camera field to vegetated field was calculated as 83% for the upper bound case (configuration d_8) and was applied to all other cases. These cropped surface maps served as the basis for wave energy analysis since wave energy density per unit area is related to local wave height η by $\mathcal{E}_w = \frac{1}{2}\rho g \eta^2$, where ρ is the density of the fluid.

In order to calculate transmission and reflection coefficients, the surface wave maps were analysed in their complex form using fast Fourier transform. We assume in our study that the imposed waves are linear, thereby allowing us to work with the 1st (fundamental) mode of the wave averaged over time:

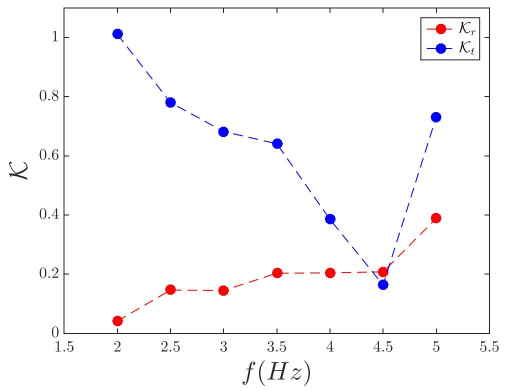

Figure 5. Variation of K_r and K_t coefficients for configuration l_2.

$$\eta_1(x, y) = \frac{2}{T}\int_0^T \eta(x, y, t)\cdot \mathrm{e}^{\mathrm{i}\omega t}\mathrm{d}t. \quad (1)$$

Finally, these transformed surface wave maps are averaged transversally (in the y-direction).

From figure 2, we can define a zone $Z1$ located before the blades as $[0, x_{\min}]$ and a zone $Z2$ located after the blades as $[x_1, x_b]$. It is assumed that the waves in each zone have the form

$$\eta(x) = \begin{cases} a\mathrm{e}^{-\mathrm{i}kx} + K_r a\mathrm{e}^{\mathrm{i}kx} & \text{in } Z1 \\ K_t a\mathrm{e}^{-\mathrm{i}kx} & \text{in } Z2. \end{cases} \quad (2)$$

Taking x_a and $x_b \in Z1$, and $x_c \in Z2$, the reflection (K_r) and transmission (K_t) coefficients can then be defined as

$$K_r = \frac{\mathrm{e}^{-\mathrm{i}kx_b} - H_1\cdot \mathrm{e}^{\mathrm{i}kx_a}}{H_1\cdot \mathrm{e}^{\mathrm{i}kx_a} - \mathrm{e}^{\mathrm{i}kx_b}} \quad (3)$$

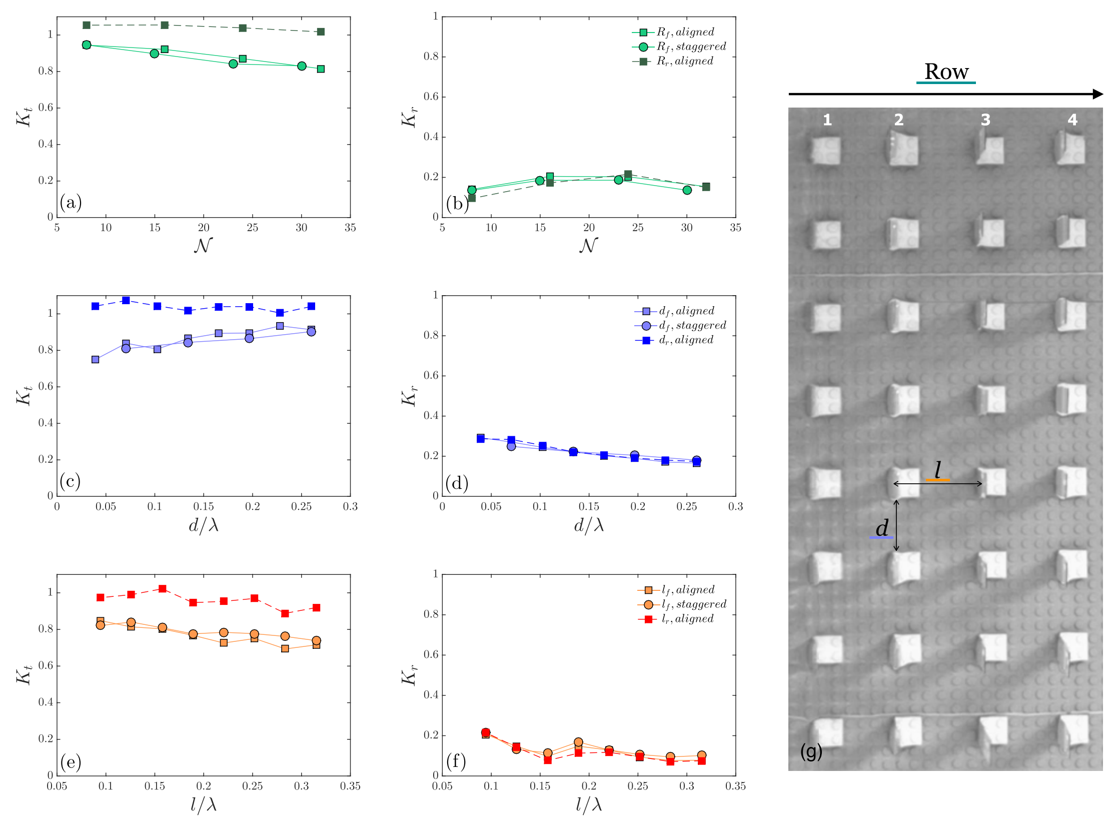

Figure 6. Proportion of power reflected K_r and transmitted K_t for an imposed frequency of 2.5 Hz, for varying parameters shown in figure (g). Configurations of increasing rows R are shown in figures (a) and (b), those of increasing spacing d are shown in figures (c) and (d), and those of increasing spacing l are shown in figures (e) and (f). Results are presented for flexible aligned (solid lines, squares), rigid aligned (dashed lines, squares), and flexible staggered (solid lines, circles) cases.

$$K_t = \frac{\mathrm{e}^{-\mathrm{i}kx_a} + K_r \cdot \mathrm{e}^{\mathrm{i}kx_a}}{H_2 \cdot \mathrm{e}^{-\mathrm{i}kx_c}} \tag{4}$$

where H_1 and H_2 are transfer functions defined as $\eta(x_b)/\eta(x_a)$ and $\eta(x_a)/\eta(x_c)$, respectively. All three points x_a, x_b, x_c were selected randomly and final coefficients were averaged over 200 iterations.

As explained previously, the canal width exceeds that of the array by a distance δ (see table 1). It is therefore worth noting that given the range of frequencies tested and the variable array widths, diffraction will be visible for cases where the total width of the array is of the order $\mathcal{O}(\lambda)$. It is the case, for example, for configuration d_1 at the resonant frequency 4.5 Hz. Nonetheless, these effects are limited, with a resulting error on the transmission coefficients of approximately 3%.

These coefficients are plotted in figure 5 over the entire range of tested frequencies for configuration l_2 (aligned, flexible case). The results show a decrease in transmission with a minimal value at 4.5 Hz, which corresponds to the natural resonant frequency of the blades measured in water. Therefore, the results for all configurations were chosen to be analysed at two bounding frequencies: 2.5 Hz (figure 6) and 4.5 Hz (figure 7). All configurations presented in table 1 are shown, and results are plotted as a function of the varied parameter: increasing number of blades $\mathcal{N}$, and increasing spacings d and l, both scaled to λ.

Results show that all configurations follow similar trends with a constant offset in the transmission coefficients between rigid (dashed lines) and flexible cases (solid lines). The value of this offset is measured around 0.2 for frequency 2.5 Hz and increases to reach values of up to 0.6 for frequency 4.5 Hz, thus showing that the flexible arrays can reduce wave damping by around 40% compared to rigid ones (see figure 7). This global observation highlights the role played by flexibility regarding wave energy transmission. It is found that as the imposed wave frequency tends towards the natural resonant frequency of the blades, these transmit less then their rigid equivalent, regardless of the spatial arrangement. This is expected since the oscillations of the blades are largest at their resonant frequency. Details on the mechanics of these oscillations will be presented in section 3.2 below. However, it is noticed that this distinction is not true regarding reflection. In fact, the curves for all three cases (rigid (dashed line), flexible aligned (squares, solid line) and flexible staggered (circles, solid line)) remain very close together, for both imposed frequencies (see figures 6 and 7), which suggests that flexibility has little influence on the reflection of waves. Furthermore, it is seen that the results of transmission and reflection coefficients are very similar between aligned and staggered configurations. In fact, most curves match exactly. This is unexpected given that in a staggered configuration, a larger number of blades are directly facing the incident

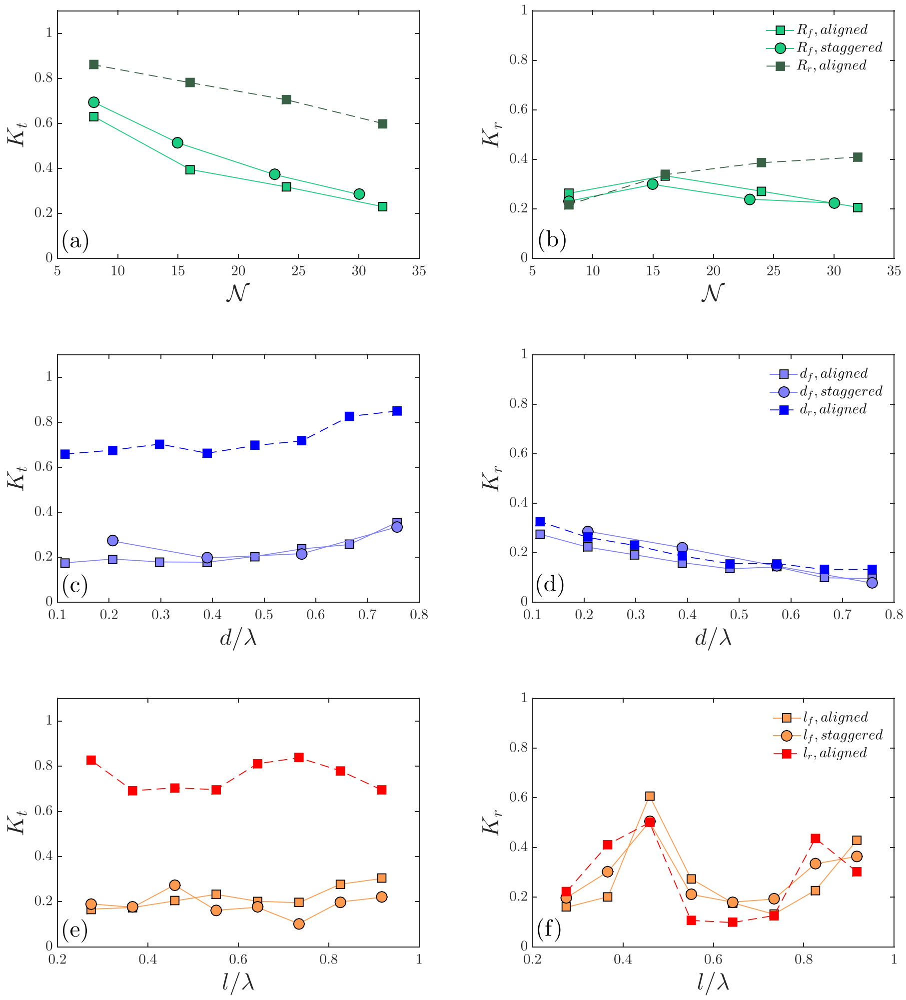

Figure 7. Proportion of power reflected K_r and transmitted K_t for an imposed frequency of 4.5 Hz, for varying parameters shown in figure 6(g). Configurations of increasing rows R are shown in figures (*a*) and (*b*), those of increasing spacing d are shown in figures (*c*) and (*d*), and those of increasing spacing l are shown in figures (*e*) and (*f*). Results are presented for flexible aligned (solid lines, squares), rigid aligned (dashed lines, squares), and flexible staggered (solid lines, circles) cases.

wave front. Yet, this result shows that the parameter l dominates the interference between rows, rather than the lateral offset of the neighbouring rows.

The results for frequency 2.5 Hz (see figure 6) show varying tendencies for each configuration. The transmission coefficient is seen to decrease as $\mathcal{N}$ increases (figure 6(a)), stabilising towards a minimal value of 0.8 beyond $\mathcal{N} = 24$ (configuration R_3). In parallel, a decrease in reflection is noticed at R_3 (figure 6(b)). This suggests that maximal efficiency regarding wave attenuation is reached with an array composed of 3 rows. In contrast, the transmission coefficient K_t for the flexible cases increases linearly with the spacing d (figure 6(c)), while the reflection coefficient K_r decreases (figure 6(d)). Both observations imply that as the array spreads out, i.e. d becomes larger, the waves interact less with the array leading to lower damping and reflection. Finally, transmission seems to remain more or less stable, regardless of the size of l (figure 6(e)), with values that fluctuate around 0.8 for the flexible cases. Similarly, reflection coefficients oscillate around 0.1 for all cases (figure 6(f)). Parameter d is therefore more influential than l at that frequency.

Figure 7 presents the same results for a wave frequency matching the natural frequency of the blades (4.5 Hz). As seen previously, increasing the number of rows leads to a decrease in transmission (figure 7(a)), reducing it by 10% for the rigid case and by 20% for the flexible cases. The collective behaviour of the flexible array would therefore benefit wave damping. An inflexion point at R_2 is noticed here again for K_r values of both flexible cases (figure 7(b)), also pointing towards an effect due to the interactions between blades. The mechanical behaviour of the array will be further discussed in the following section 3.2.

As before, increasing d increases transmission coefficients while the reflection coefficients decrease (figures 7(c) and (d)). It should however be noted that the increase in K_t is not quite linear and appears to sharpen starting from $d/\lambda = 0.5$ for both flexible cases. As a mirror, the reflection decreases sharply for lower values of d. This implies that this specific space size serves as a point of inflexion regarding the dominance of transmission versus reflection. In the case of a flexible aligned configuration, transmission overtakes reflection beyond spacing $d < \lambda/2$.

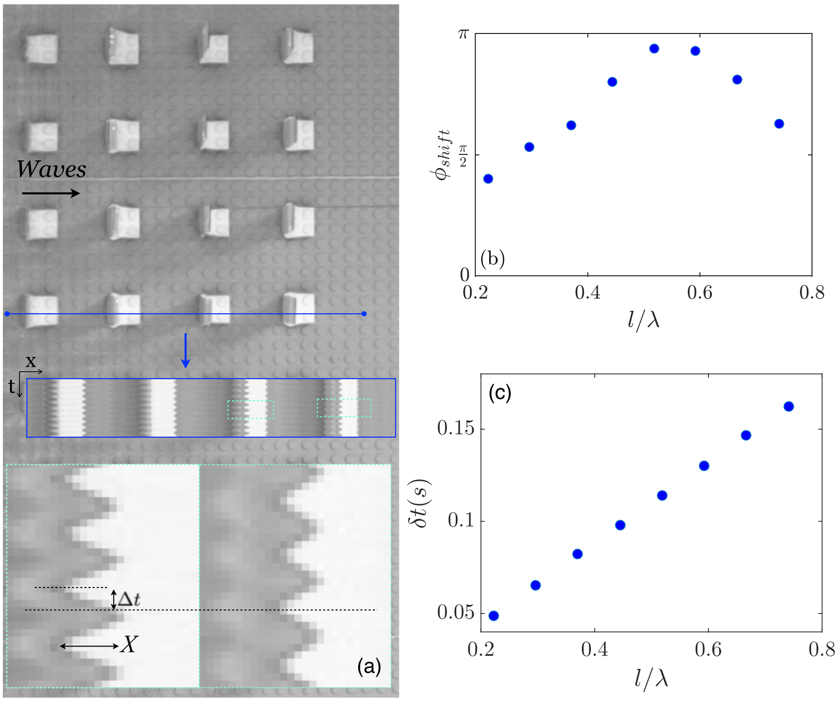

Figure 8. Tracking blade oscillations. Tracking set-up (a). Average phase shifts between rows as a function of the spacing l/λ (b). Time delay $\delta(t)$ between oscillation time shifts Δt and wave travel time t between two rows, as a function of the spacing l/λ (c). Example taken on configuration l at frequency 4 Hz.

Finally, increasing the size of l shows oscillatory variations in both transmission and reflection (figures 7(e) and (f)), with higher points near $l/\lambda = \{0.5; 1\}$ and lower K_t points near $l/\lambda = \{0.25; 0.75\}$, for flexible cases. The oscillations in K_t are mirrored in the case of rigid blades. This is due to the interference between incident and reflected waves within the array. Indeed, when a regular arrangement of obstacles such as ours in subject to incoming waves, crystallographic behaviours can be considered. Bragg's law states the condition for constructive or destructive interferences of incident waves as $2l \sin\theta = n\lambda$, with l being the spacing between two lattices and θ the incident angle of waves. When n is an integer, then the reflected waves are perfectly in phase with the incident wave, thereby building large amplitudes in the resulting waves. In our case, $\theta = \pi/2$, which simplifies the condition as $n = 2l/\lambda$. We therefore have $n = 1$ for $l/\lambda = 0.5$ and, similarly, $n = 2$ for $l/\lambda = 1$. This explains the large reflection coefficients obtained for these two points. In the case of rigid blades, these oscillations are mirrored in the transmission coefficient, due to the fact that this large reflected energy is not transmitted. While the same observation can be made for the flexible cases regarding reflection, this does not hold for transmission. In this case, although the resulting amplitudes are larger, the wave forcing is in fact lower leading to reduced blade oscillations (see figure 9).

3.2. Tracking

The second part of the experiment involved tracking the movement of the blades. A spatio-temporal stacking of each blade was performed, as shown in figure 8(a), to determine both the amplitude and the phase of their oscillations. The time shifts Δt of the blade oscillation peaks were directly measured and converted into phase shifts, with $\phi_{\text{shift}} = (\Delta t/T)2\pi$, where T is the oscillation period in seconds (see figure 8(b)). These oscillation time delays Δt were compared to the time taken for the wave to travel between blades $t = l/v_\phi$, where v_ϕ is the phase velocity of the wave, equal to $f\lambda$. Figure 8(c) shows this relationship is linear, which suggests that the phase shifts observed between rows depend directly on the time needed for the waves to travel between them.

The oscillation amplitudes X were also directly measured for each blade and the average $\bar{X}$ of each row is presented in figure 9, for all tests. In general, results show that for all cases, amplitudes $\bar{X}$ are largest in the first row, and decrease as we travel further into the array, due to both natural dissipation and to the interaction with each row.

Figures 9(a) and (b) show the variation of these amplitudes as a function of the number of rows for configurations R_{aligned} and $R_{\text{staggered}}$, respectively. In the case of an aligned configuration, the average amplitude of each row decreases when it remains constant for the staggered configuration, regardless of the number of rows present. This highlights the influence of the reflected waves within the array, depending on their longitudinal alignment. Indeed, it is suggested by Sarkar *et al* (2014) that for inline configurations, the presence of neighbouring oscillating structures in the x-direction (longitudinal direction) provides strong destructive interferences, leading to limited oscillating amplitudes. This is coherent with our observation.

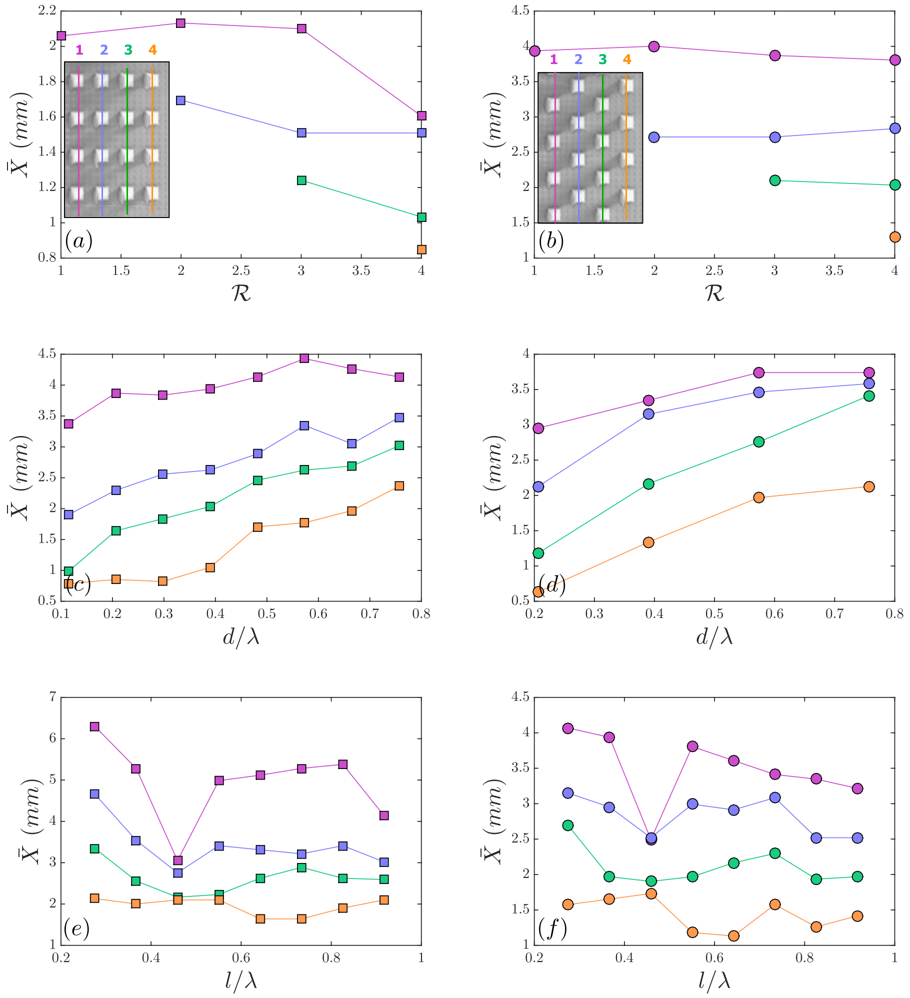

Figure 9. Comparison of average oscillating amplitude $\bar{X}$ for each row of blades between aligned (squares) and staggered (circles) cases. Results for configurations R_{aligned} (a) and $R_{\text{staggered}}$ (b), d_{aligned} (c) and $d_{\text{staggered}}$ (d), l_{aligned} (e) and $l_{\text{staggered}}$ (f).

The following two figures 9(c) and (d) plot the mean variations of amplitudes for each row belonging to configurations d_{aligned} and $d_{\text{staggered}}$, respectively. Both arrangements provide similar results, demonstrating that amplitudes increase with spacing d. Once again, Sarkar *et al* (2014) predict that as oscillating structures are spread out, these tend to behave like individual systems with larger movements. Yet, it should be noted that this increase is slowed down as d becomes larger, especially in the case of a staggered arrangement (figure 9(d)). This lower slope mirrors the steeper slope previously observed in the transmission coefficients (see figure 7(c)), found to occur for $d > \lambda/2$.

Finally, the amplitude variations for configurations l_{aligned} and $l_{\text{staggered}}$ are presented in figures 9(e) and (f), respectively. One can notice very similar behaviour between the two arrangements, with a narrow point of oscillation at $l = \lambda/2$. This confirms the observations made for both transmission and reflection coefficients in figures 7(e) and (f). As mentioned before, the corresponding spatial arrangement of the blades cause wave interferences within the array to be detrimental towards blade oscillations.

Tracking the movement of the blade tips was also used to determine the amount of energy absorbed through the movement of the flexible blades. Unlike their rigid equivalent, the Mylar blades are able to bend and oscillate as the wave fluid passes through each row of the array. This is caused by the movement of the surface particles, that oscillate with a velocity:

$$u(x,z,t) = \eta\omega\frac{\cosh k(h+z)}{\sinh kh}\cos(kx-\omega t). \quad (5)$$

For fixed t and x, we obtain the following expression describing the amplitude of the horizontal component of the velocity, function of z:

$$u_a(z) = \eta\omega\frac{\cosh k(h+z)}{\sinh kh}. \quad (6)$$

This water particle horizontal velocity component was calculated using equation (6) along the water column $h = 8$ cm for all wave frequencies tested.

The energy lost due to these oscillations is done through two mechanisms. Part of it is transferred into mechanical energy of bending (absorbed energy $\mathcal{E}_a$) and part of it is lost to the fluid due to the drag caused by the interaction between the blades and the surrounding fluid (dissipated energy $\mathcal{E}_d$).

We model our blades as simple cantilevered beams and assume linear theory to be valid given the small oscillations observed (ranging from 2–8 mm in amplitude X). If we assume that each blade oscillates in its first mode of deformation, the local deflected shape v_1 for each beam section is given by (see e.g. Volterra and Zachmanoglou (1965)) (figure 1(c))

$$v_1(z)=\frac{1}{2}((\cos(k_1z)-\cosh(k_1z)) + \left(\frac{-\cos(k_1h_s)-\cosh(k_1h_s)}{\sin(k_1h_s)-\sinh(k_1z)}\right)(\sin(k_1z)-\sinh(k_1z))) \tag{7}$$

where h_s is the total length of the beam, k_1 is the first deformation mode coefficient. The local position of the beam section is described by the function $x(z,t)=\underline{v}_1(z)\cdot\underline{X}(t)$, given small deformations. Our blade becomes a damped oscillator for which the equation of movement is then

$$m\ddot{x}+kx=-\gamma\dot{x}. \tag{8}$$

This damping term must be further decomposed into an internal damping restoring force of the blade and the external drag damping force exerted by the external fluid. This second term is in fact nonlinear term related to the relative velocity of the blade, u_r. However, the experimental data matches a linear fit, which suggests that a linear term can be assumed in this case. The damping force of our blade becomes $\gamma_{\text{in}}\dot{x}+\gamma_{\text{ext}}u_r$. The relative velocity u_r of our blade is determined using the tracking data (amplitude X measured over a half period $T/2$) and the horizontal velocity of the fluid calculated from equation (5) above:

$$u_r(z)=u_a(z)-\dot{x}(z). \tag{9}$$

The mechanical power of the oscillating blade must equal the damped energy flux, so that

$$\mathcal{P}=(-\gamma_{\text{int}}\dot{x}\cdot\dot{x})+(-\gamma_{\text{ext}}u_r\cdot u_r). \tag{10}$$

Given $\Gamma=\frac{\gamma}{2m}$ from equation (8), this power can thus be calculated from the damping coefficients Γ_{int} and Γ_{ext}, the blade velocity $\dot{x}$, the relative velocity u_r, the mass of the blade m and the added mass of displaced fluid m_a, as derived in

$$\mathcal{P}=2[\Gamma_{\text{int}}(m+m_a)\dot{x}^2+\Gamma_{\text{ext}}(m+m_a){u_r}^2] \tag{11}$$

with $\Gamma_{\text{int}}=1.7\ \text{s}^{-1}$ and $\Gamma_{\text{tot}}=6.4\ \text{s}^{-1}$, where $\Gamma_{\text{ext}}=\Gamma_{\text{tot}}-\Gamma_{\text{in}}$. These two values were measured from free oscillation tests by fitting an exponential curve of the form $A_0\text{e}^{-\Gamma t}+c$ to the range of amplitudes observed in the experiments (8 mm–2 mm, see figure 9). These were obtained with 99% fitting precision using the least-squares method.

This power can be further separated between the internally absorbed power due to the work of the blade ($\mathcal{P}_a$), and the externally dissipated power due to the relative movement of the surrounding fluid ($\mathcal{P}_d$). The expressions are provided in

$$\mathcal{P}_a=2\Gamma_{\text{int}}\left(\int_0^{h_s}\mu_s\left(\frac{\text{d}[v_1(z)X(t)]}{\text{d}t}\right)^2\text{d}z + \int_0^h\mu_l\left(\frac{\text{d}[v_1(z)X(t)]}{\text{d}t}\right)^2\text{d}z)\right) \tag{12}$$

$$\begin{aligned}\mathcal{P}_d&=2\Gamma_{\text{ext}}\left(\int_0^h\mu_s\left(u_a(z)-\frac{\text{d}[v_1(z)X(t)]}{\text{d}t}\right)^2\text{d}z + \int_0^h\mu_l\left(u_a(z)-\frac{\text{d}[v_1(z)X(t)]}{\text{d}t}\right)^2\text{d}z\right)\\&=2\Gamma_{\text{ext}}\left(\int_0^h(\mu_s+\mu_l)\left(u_a(z)-\frac{\text{d}[v_1(z)X(t)]}{\text{d}t}\right)^2\text{d}z\right)\end{aligned} \tag{13}$$

where μ_s and μ_l are the linear masses of the solid and of the displaced liquid, respectively.

The total incoming energy of the waves was calculated from the surface wave maps using the relationship $\mathcal{E}_w=\frac{1}{2}\rho g\eta^2$ defined previously. This provides the energy flux per unit area of the canal. Multiplying this energy by the wave group velocity v_g (which is equal to half the phase velocity v_ϕ in the deep water conditions of the present experiments) gives the wave energy flux per unit width:

$$\mathcal{P}_w=\mathcal{E}_w\cdot v_g. \tag{14}$$

In our case, we wish to compare the total available incident wave energy to the energy lost in our vegetated area. Therefore, the wave energy flux must be multiplied by the width of our area along with the number of waves within the area (ratio L/λ) in order to obtain the total wave energy flux entering our array

$$\mathcal{P}_{\text{tot}}=\mathcal{P}_w\cdot W=\frac{1}{2}\rho g\eta^2v_gW\frac{L}{\lambda}. \tag{15}$$

Note that due the variability of η between experiments, average values were taken for each set of experiments (e.g. $l_{\text{staggered}}$), based on the previously calculated K_r coefficients, as follows: $\eta=\eta(x_{\text{min}})=\eta(x_0)/(1+K_r)$ (see figure 2).

In parallel, the absorbed power of each individual blade is calculated using equation (12). The sum of individual $\mathcal{P}_a$ therefore provides the total power absorbed by our array as follows

$$\mathcal{P}_a=\sum_{i=1}^{\mathcal{N}}(\mathcal{P}_a)_i \tag{16}$$

where $\mathcal{N}$ is the total number of blades. The total dissipated power $\mathcal{P}_d$ was calculated in the same manner. It was then possible to estimate the proportion of the incoming power that was absorbed by the array using a coefficient $K_a=\mathcal{P}_a/\mathcal{P}_{\text{tot}}$, along with the proportion of the incoming power that was dissipated and lost to the fluid $K_d=\mathcal{P}_d/\mathcal{P}_{\text{tot}}$. The sum of these two values therefore quantifies the amount of power

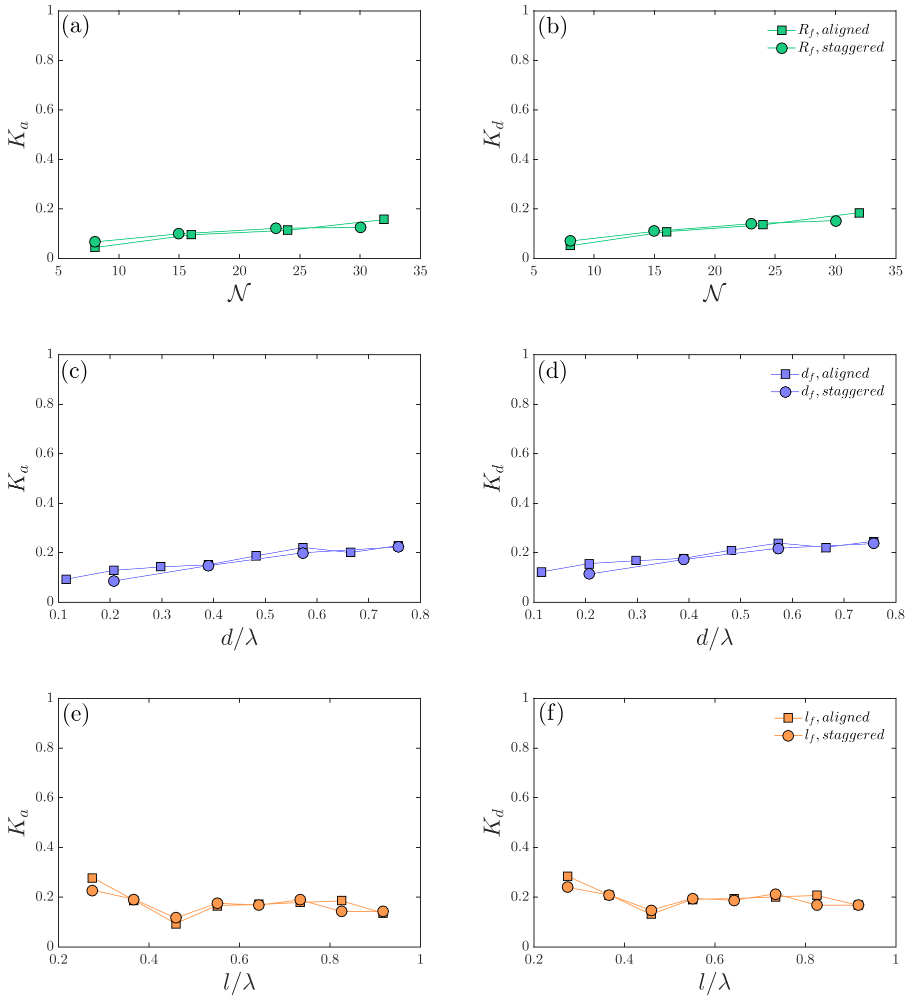

Figure 10. Proportion K_a of power absorbed by the blades through deflection (left) and proportion K_d of power dissipated by the surrounding fluid (right), as calculated from equations (12) and (13) using blade oscillation measurements given in figure 9. Results are presented for both aligned (squares) and staggered (circles) configurations R, d and l (from top to bottom), at frequency 4.5 Hz.

that is dissipated both internally and externally (K_m), due to the bending motion of the blades.

The results of these calculations are presented in figure 10 for all configurations at the excitation frequency of 4.5 Hz. The total amount of absorbed and dissipated power depends, of course, on the total number of blades present in the array and the results for configuration R in figures 10(a) and (b) show a maximal value of around 20% of absorbed power with an equivalent amount dissipated to the fluid. This amounts to a total loss of power within the array of around 40%, which corresponds to the difference in transmission between flexible and rigid cases (see figure 7). Similarly, increasing d also shows an increase in absorbed and dissipated power within the array, due to the increase in oscillation amplitudes seen in figures 9(b) and (c). Here again, the sum of K_a and K_d for configuration l_8 match the difference in transmission between the flexible array and its rigid equivalent as presented in figures 7(b) and (c), and this is overall the case for the other configurations of d. It is also noted that unlike wave damping, increasing d favours energy absorption. Finally, recalling figures 7(e) and (f), the transmission coefficients curves for configurations l and $l_{\text{staggered}}$ mirror the tendencies seen here for K_a and K_d (figures 10(e) and (f)). Once again, the troughs found at $l/\lambda = 0.5$ are caused by the lower amplitudes of oscillation of the blades due to wave interferences within the array. This lower amount of energy dissipation is therefore seen as a higher amount of transmission in figure 7.

4. Conclusion

This experimental study explored the role of flexibility and spatial distribution regarding wave dissipation and potential energy harvesting through a kelp-bed inspired array of partially submerged flexible beams. The spacing distances l between rows and d within rows were varied, along with the number of rows, and aligned and staggered arrangements were compared for each configuration. It was demonstrated that for both rigid and flexible blades, transmitted power reduces with the number of blades, increases with parameter d, and is globally independent of the spacing parameter l, i.e. maximal dissipation through the system is reached with large, dense arrays. Unexpectedly, reflection was not found to increase steadily. Instead, it was seen to decrease slowly for arrays larger than two rows, as well as with large values of d, but it demonstrated strong fluctuations depending on parameter l/λ, which are caused by interferences internal to the array.

Wave energy damping was much improved when flexible beams were used, with a decrease in transmission of around 40%, compared to their rigid equivalent. This is consistent with previous field studies, which show flexible aquatic plants to play an essential role in erosion control. Moreover, it was demonstrated that the blades absorb an additional amount of energy through mechanical bending (around 20% of the total incoming energy), which represents in a sense the potential amount of energy that could be harvested into useful electricity. While this quantity remains limited compared to existing WEC devices, it relates to a minimalistic system, without any form of neither device nor array optimisation, and its value could certainly be improved by using more advanced systems. Furthermore, WEC arrays have not yet demonstrated strong effects on wave damping. The results presented in this paper demonstrate the potential for combining applications of an array of flexible oscillating blades to both wave damping and wave energy harvesting.

This study was focused on the influence of flexibility on wave energy distribution and was limited to simple cases: simple blade geometry and regular waves were used. Additional studies need to be undertaken with more complex systems to understand the influence of these fixed parameters on the energy harvesting capacity of a blade array. Further work is also needed to fully understand the energy distribution of the incoming waves. The wave energy has been shown here to be shared between transmission, reflection and mechanical damping, along with an additional loss representing up to 40% of the total initial energy in certain cases. The diffraction of waves within the array along with the drag imposed by the array are at least partly responsible for this loss and should be further investigated.

Acknowledgments

We acknowledge support from the Franco-Argentinian International Associated Laboratory in the Physics and Mechanics of Fluids (LIA PMF-FMF, CNRS France, CONICET Argentina) and from the BEC. AR program (Argentina). We are grateful to the *Manipulation d'Ondes de Surface* team at PMMH, in particular Eduardo Monsalve and Thomas Humbert, for allowing us to use their wave tanks and providing valuable help with the surface wave analysis, and Agnès Maurel for fruitful discussions.

ORCID iDs

C Nové-Josserand https://orcid.org/0000-0001-9316-6453
R Godoy-Diana https://orcid.org/0000-0001-9561-2699
B Thiria https://orcid.org/0000-0002-2449-1065

References

Anderson M E and Smith J M 2014 Wave attenuation by flexible, idealized salt marsh vegetation *Coast. Eng.* **83** 82–92

Anderson M E, Smith J M and McKay S K 2011 Wave dissipation by vegetation *Coastal and Hydraulics Engineering Technical Note ERDC/CHL CHETN-I-82* (U.S. Army Engineer Research and Development Center, Vicksburg, MS) (https://doi.org/10.21236/ad1003881)

Asano T, Deguchi H and Kobayashi N 1993 Interaction between water waves and vegetation *23rd Int. Conf. Coastal Engineering* pp 2709–23

Augustin L N, Irish J L and Lynett P 2009 Laboratory and numerical studies of wave damping by emergent and near-emergent wetland vegetation *Coast. Eng.* **56** 332–40

Barsu S, Doppler D, Jerome J J S, Rivière N and Lance M 2016 Drag measurements in laterally confined 2D canopies: reconfiguration and sheltering effect *Phys. Fluids* **28** 107101

Buck B H and Buchholz C M 2005 Response of offshore cultivated laminaria saccharina to hydrodynamic forcing in the north sea *Aquaculture* **250** 674–91

Chang C W, Liu P L F, Mei C C and Maza M 2017a Modeling transient long waves propagating through a heterogeneous coastal forest of arbitrary shape *Coast. Eng.* **122** 124–40

Chang C W, Liu P L F, Mei C C and Maza M 2017b Periodic water waves through a heterogeneous coastal forest of arbitrary shape *Coast. Eng.* **122** 141–57

Dalrymple R A, Kirby J T and Hwang P A 1984 Wave diffraction due to areas of energy dissipation *J. Waterway Port Coast. Ocean Eng.* **110** 67–79

De Langre E 2008 Effects of wind on plants *Annu. Rev. Fluid Mech.* **40** 141–68

Denny M and Gaylord B 2002 The mechanics of wave-swept algae *J. Exp. Biol.* **205** 1355–62

Dittrich A and Jarvela J 2005 Flow-vegetation-sediment interaction *Water Engineering Research* **6** 123–30

Dubi A and Tørum A 1995 Wave damping by kelp vegetation *Coast. Eng. 1994* pp 142–56

Dubi A and Torum A 1996 Wave energy dissipation in kelp vegetation *Coast. Eng. Proc.* 1 2626–39

Duclos G and Clément A H 2004 Wave propagation through arrays of unevenly spaced vertical piles *Ocean Eng.* **31** 1655–68

Feagin R A, Lozada-Bernard S M, Ravens T M, Möller I, Yeager K M and Bairs A H 2009 Does vegetation prevent wave erosion of salt marsh edges? *Proc. Natl Acad. Sci.* **106** 10109–13

Guo X, Wang B and Mei C C 2014 Flow and solute transport through a periodic array of vertical cylinders in shallow water *J. Fluid Mech.* **756** 903–34

Henry P, Myrhaug D and Aberle J 2015 Drag forces on aquatic plants in nonlinear random waves plus current *Estuarine Coast. Shelf Sci.* **165** 10–24

Kagemoto H and Yue D K P 1986 Interactions among multiple three-dimensional bodies in water waves: an exact algebraic method *J. Fluid Mech.* **166** 189–209

Kakuno S and Liu P L 1993 Scattering of water waves by vertical cylinders *J. Waterway Port Coast. Ocean Eng.* **119** 302–22

Kamath A, Bihs H, Chella M A and Arntsen Ø A 2015 CFD simulations to determine wave forces on a row of cylinders *Proc. Eng.* **116** 623–30

Keulegan G H and Carpenter L 1958 Forces on cylinders and plates in an oscillating fluid *J. Res. Natl Bur. Stand.* **60** 423

Koehl M A R 1984 How do benthic organisms withstand moving water? *Am. Zool.* **24** 57–70

Koehl M A R and Wainwright S A 1977 Mechanical adaptations of a giant kelp *Limnol. Oceanogr.* **22** 1067–71

Leclercq T and de Langre E 2016 Drag reduction by elastic reconfiguration of non-uniform beams in non-uniform flows *J. Fluids Struct.* **60** 114–29

Linton C M and Evans D V 1990 The interaction of waves with arrays of vertical circular cylinders *J. Fluid Mech.* **215** 549–69

Liu P L F, Chang C W, Mei C C, Lomonaco P, Martin F L and Maza M 2015 Periodic water waves through an aquatic forest *Coast. Eng.* **96** 100–17

Løvås S M and Tørum A 2001 Effect of the kelp laminaria hyperborea upon sand dune erosion and water particle velocities *Coast. Eng.* **44** 37–63

Luhar M and Nepf H M 2016 Wave-induced dynamics of flexible blades *J. Fluids Struct.* **61** 20–41

Manca E, Cáceres I, Alsina J M, Stratigaki V, Townend I and Amos C L 2012 Wave energy and wave-induced flow reduction by full-scale model Posidonia oceanica seagrass *Cont. Shelf Res.* **50–1** 100–16

Massel S R, Furukawa K and Brinkman R M 1999 Surface wave propagation in mangrove forests *Fluid Dyn. Res.* **24** 219–49

Mei C C, Chan I C and Liu P L F 2014 Waves of intermediate length through an array of vertical cylinders *Environ. Fluid Mech.* **14** 235–61

Mei C C, Chan I C, Liu P L F, Huang Z and Zhang W 2011 Long waves through emergent coastal vegetation *J. Fluid Mech.* **687** 461–91

Moisy F, Rabaud M and Salsac K 2009 A synthetic schlieren method for the measurement of the topography of a liquid interface *Exp. Fluids* **46** 1021

Möller I *et al* 2014 Wave attenuation over coastal salt marshes under storm surge conditions *Nat. Geosci.* **7** 727–31

Nepf H M 2012 Flow and transport in regions with aquatic vegetation *Annu. Rev. Fluid Mech.* **44** 123–42

Sarkar D, Renzi E and Dias F 2014 Wave farm modelling of oscillating wave surge converters *Proc. R. Soc.* A **470** 2167

Vogel S 1984 Drag and flexibility in sessile organisms *Am. Zool.* **24** 37–44

Vogel S 1989 Drag and reconfiguration of broad leaves in high winds *J. Exp. Bot.* **40** 941–8

Volterra E and Zachmanoglou E C 1965 Dynamics of vibrations *Dynamics of Vibrations* vol 1 (Columbus, OH: C.E. Merrill Books)

Zeller R B, Weitzman J S, Abbett M E, Zarama F J, Fringer O B and Koseff J R 2014 Improved parameterization of seagrass blade dynamics and wave attenuation based on numerical and laboratory experiments *Limnol. Oceanogr.* **59** 251–66